J. Fluid Mech. (2010), *vol.* 655, *pp.* 258–279.
doi:10.1017/S0022112010000868

Formation and decay of coherent structures in pipe flow

JIMMY PHILIP† AND JACOB COHEN
Faculty of Aerospace Engineering, Technion-I.I.T., Haifa 32000, Israel

(Received 29 April 2009; revised 7 February 2010; accepted 10 February 2010;

Experimental investigation of the generation and decay of coherent structures, namely, streaks (accompanied by a counter-rotating vortex pair) and hairpin vortices in pipe flow, is carried out by artificial injection of continuous disturbances. Flow visualization and velocity measurements show that for small amplitudes of disturbances (v_0) streaks are produced, and increasing v_0 produces instability waves on the streaks, which further break down into an array of hairpin vortices. However, the streaks and hairpins decay along the downstream direction (X). In fact, the critical value of v_0 required for the initiation of hairpins at a given Re (Reynolds number) varies with the streamwise distance (in contrast to the previously found scaling of $v_0 \sim Re^{-1}$, valid only close to the location of injection, i.e. smaller X). This is a consequence of the decay of the coherent structures in the pipe. Moreover, the hairpins have been found to decay more slowly with increasing Re. Measurements of energy in the cross-sectional plane of the pipe, and maps of disturbance velocity at various X-locations show the transient growth and decay of energy for relatively low v_0. For higher v_0 and Re the energy has been seen to increase continuously along the length of the pipe under observation. Owing to the increase in the cross-sectional area occupied by the disturbance along the X-direction, it is observed that energy can transiently increase even when the total disturbance magnitude is decreasing. Observing the similarity of the present work and other investigations wherein decay of turbulence in pipe flow is found, a schematic illustration of the transition surface for pipe flow on a v_0–Re–X, three-dimensional coordinate system is presented.

1. Introduction

Many of the recent developments in pipe flow transition are summarized in the review article by Eckhardt *et al.* (2007) and in the special issue of *Phil. Trans. R. Soc.* A edited by Eckhardt (2009), commemorating the 125th anniversary of Reynolds' seminal paper (Reynolds 1883) on pipe flow transition. This section highlights the salient features of this long-standing problem. Experiments show that flow in a pipe can be kept laminar to very high Reynolds numbers ($Re = U_{cl} R_0/\nu$, where U_{cl} is the centreline velocity of the incoming laminar flow, R_0 the radius of the pipe and ν the kinematic viscosity of the fluid) up to 10^5 (Pfenniger 1961), in accordance with the inability to find unstable waves by linear stability theory (e.g. Meseguer & Trefethen 2003). However, the flow becomes turbulent for finite amplitude

---

† Present Address: Laboratoire d'Hydrodynamique (LadHyX), École Polytechnique, 91128 Palaiseau, France. Email address for correspondence: jimmyp@aerodyne.technion.ac.il

disturbances, the value of which decreases with increasing *Re* (e.g. Wygnanski & Champagne 1973; Hof, Juel & Mullin 2003; Peixinho & Mullin 2007).

The failure of normal-mode linear stability analysis to predict unstable waves in pipe flow has led to the search for other scenarios to explain energy amplification. The linear transient growth scenario is the one in which the disturbance increases transiently and may reach a significant amplitude that can trigger nonlinear mechanisms before its long-time decay due to viscous effects (e.g. Reshotko & Tumin 2001; Schmid 2007). It has been found by Schmid & Henningson (1994) that the initial structure which amplifies the most is that of a steamwise independent counter-rotating vortex pair (CVP) generating streaks. In fact, this mechanism is governed by a pair of almost parallel two least stable modes, as demonstrated by Ben-Dov, Levinski & Cohen (2003). Numerical simulations have shown that these streaks undergo secondary instability (Zikanov 1996) and can lead to transition to turbulence (Meseguer 2003) in pipe flow.

Streaks (produced via CVPs) and hairpin vortices are the coherent structures which are a common feature of all turbulent boundary layers (e.g. Kline *et al.* 1967; Robinson 1991). These structures have been observed recently in turbulent (Guala, Hommema & Adrian 2006) and transitional (Mellibovsky & Meseguer 2007) pipe flows. It is of interest to note that the streaky structures are also part of the exact travelling wave solutions found by Hof *et al.* (2004), Wedin & Kerswell (2004) and others. Hairpin vortices have been observed by Peixinho & Mullin (2007) in pipe flow while generating disturbance with a push–pull mechanism. They note that for small perturbations the hairpins decayed in their pipe.

Numerical investigations have shown that pipe flow turbulence consists of transients (Brosa 1989) and that it exhibits a chaotic nature (Faisst & Eckhardt 2004). Experimental evidence for such a scenario being present in pipe flow has been found by Hof *et al.* (2006) and Peixinho & Mullin (2006).

In the present work a systematic experimental investigation of coherent structures, i.e. streaks (and the accompanying CVPs) and hairpins, produced artificially by introducing a steady and continuous disturbance in a pipe flow is presented. It includes the formation and breakdown of the coherent structures and their decay along the downstream direction. As mentioned above, streaks are formed due to a linear process and hairpins are a result of nonlinearity (e.g. Suponitsky, Cohen & Bar-Yoseph 2005). This distinction will be taken into consideration when discussing the results further below. Experimental set-up and measurement techniques are described in § 2. Section 3 presents results pertaining to flow visualization and velocity measurements along with the associated kinetic energy, its transient growth and growth/decay along the streamwise direction. Results of instability caused by streaks and the role of streamwise distance in pipe flow transition are discussed in § 4. Final conclusions are drawn in § 5.

2. Experimental set-up

The pipe flow facility, standing vertically consists of two flow circuits, one for the base flow and another one for the disturbance. Figure 1 describes the various components associated with both circuits. For the base flow, water is stored in an overhead tank of 30 l capacity. The flow passes through a honeycomb and then through a smooth converging nozzle before entering the circular glass pipe having an inner radius (R_0) of 0.98 cm, a thickness of 0.12 mm and a total length of 230 R_0. It is mentioned here that this relatively short pipe is sufficient for our studies concerned

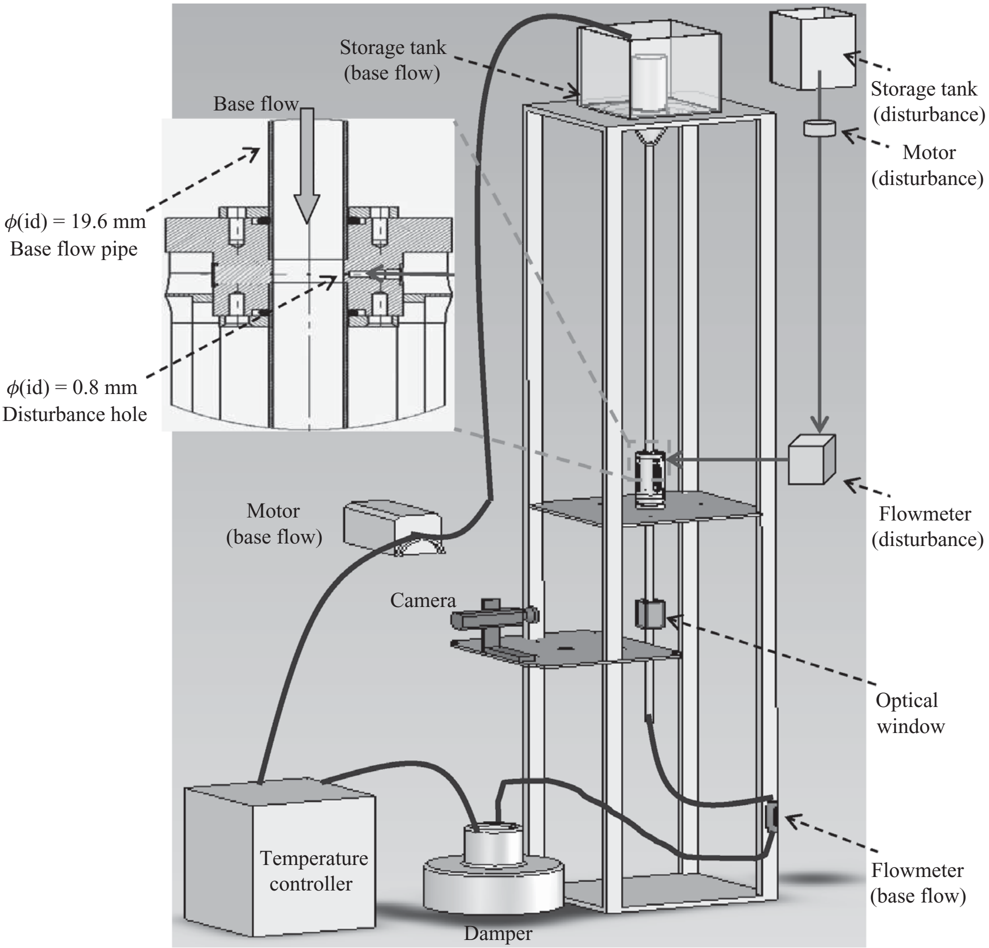

FIGURE 1. The overall experimental set-up for pipe flow. The inset shows the cross-sectional view of the location of disturbance injection.

with the linear (streak) to nonlinear (hairpin) state transition, which is evident from a previous work on ‘channel flow’ (Philip, Svizher & Cohen 2007) on the generation of hairpin vortices and the corresponding investigation of scaling laws. Therein, it is shown that the transient growth process depends on the product $v_0 t$ (where t is time and v_0, the initial amplitude of the disturbance), and therefore the same transient growth can be achieved at much shorter times (or X), if v_0 is increased.

Water coming from the pipe exits at the bottom into a damper (to damp any fluctuations remaining in the flow), and then to a temperature controller (which maintains the temperature of water to $\pm 0.1^\circ$ C). The circuit is closed by the peristaltic motor which pumps the water back into the overhead tank. It is noted that, due to the presence of the damper and overhead tank, the downstream boundary conditions of the pipe (including the various tubing) have not been observed to cause any effect on the results presented. The flow rate can be controlled by changing the r.p.m. of the motor, which translates to maintaining a laminar flow for Re within the range of 250–3000 $\pm$ 1 %. The values of Re presented below are the mean values of the measurements. Considering the uncertainty mentioned in the Re, it could be rounded to the last significant digit.

The disturbance flow is an open loop facility (unlike the base flow), wherein a water-soluble dye is mixed with water and held in a small overhead tank. The mixture is pumped through a small motor and after passing through a flow meter, metering valve and a solenoid valve (which can be controlled by computer) it is injected into the base flow at a downstream distance of about $114\,R_0$, where the flow is close to fully developed (the development of base flow is discussed later in association with figure 3). The disturbance is introduced into the base flow using a custom made injection system, a section of which is shown in the inset of figure 1. The system is designed such that there would be optical access for visualization beginning as close as possible to the injection point ($\sim 1.5\,R_0$). The injection hole has an inner diameter of 0.8 mm and the flow rates (Q_{inj}) range from 0.5 to 7.0 ml min^{-1}. The parameter describing the disturbance flow is $v_0 = Q_{inj}/(S_{inj}\,U_{cl})$, where S_{inj} is the cross-section area through which the disturbance is injected. The ratio of the volume flux of disturbance to base flow used in the present investigation is between 0.17% and 0.66 %. Flow visualization is accomplished by using a digital camera and a strong incandescent light source. Two perpendicular views of coherent structures are obtained at the same time on the camera by fixing an inclined mirror close to the pipe. The two views cannot be focused perfectly on the camera because the distance between the two actual images in the physical plane and image plane is different. Moreover, to get a good picture quality the aperture is wide open which decreases the depth of focus. So for the precise observation of the hairpin evolution, the camera was focused more on the front view where heads of the hairpins could be observed (e.g. figures 4 and 8). All the experiments begin by running the base flow for an initial period of time until the temperature reaches a nominal value of 21.5° C.

Velocity measurements are accomplished using the technique of Particle Image Velocimetry (PIV). The PIV system is a commercial one, purchased from TSI Incorporated, with a dual Nd:YAG laser of 150 mJ pulse^{-1}, 532 nm and a maximum of 15 Hz pulse rate. In the present experiments the laser is always used below its maximum available energy. The base flow is seeded for the purpose of PIV with particles with a mean diameter of about 10 μm. For obtaining velocity fields of the disturbance, the secondary flow is also seeded (containing the same particles as the base flow). This caused slight clogging in the motor used for pumping the fluid (in the flow visualization), resulting in abrupt variations in v_0. To overcome this, another more robust injection system is build, sketched in figure 2(a). It employs a plunger/syringe which is filled with the disturbance fluid (with the seeding particles) and using a computer-controlled linear motion traverse can inject the continuous disturbance into the base flow. Once the whole fluid is injected, the syringe automatically fills itself by travelling in the reverse direction and is ready for the next round of injection. Even though the traverse could move at an accuracy of better than 1 μm, to minimize any remaining fluctuations in the disturbance due to the motion of the traverse, a small fluctuation damping system is also built. It is placed just before the location where the disturbance enters the pipe, and is shown in the inset for figure 2(a). It is a container (in the present case a syringe) with part filled with the disturbance fluid and the rest with air. The air provides the required damping, if any is necessary. The advantage of using a syringe is the possibility of changing the ratio of the air–disturbance volume.

PIV images are taken when the plunger (or the main syringe) has been working for some time to avoid any initial transient effects and to obtain a continuous disturbance.

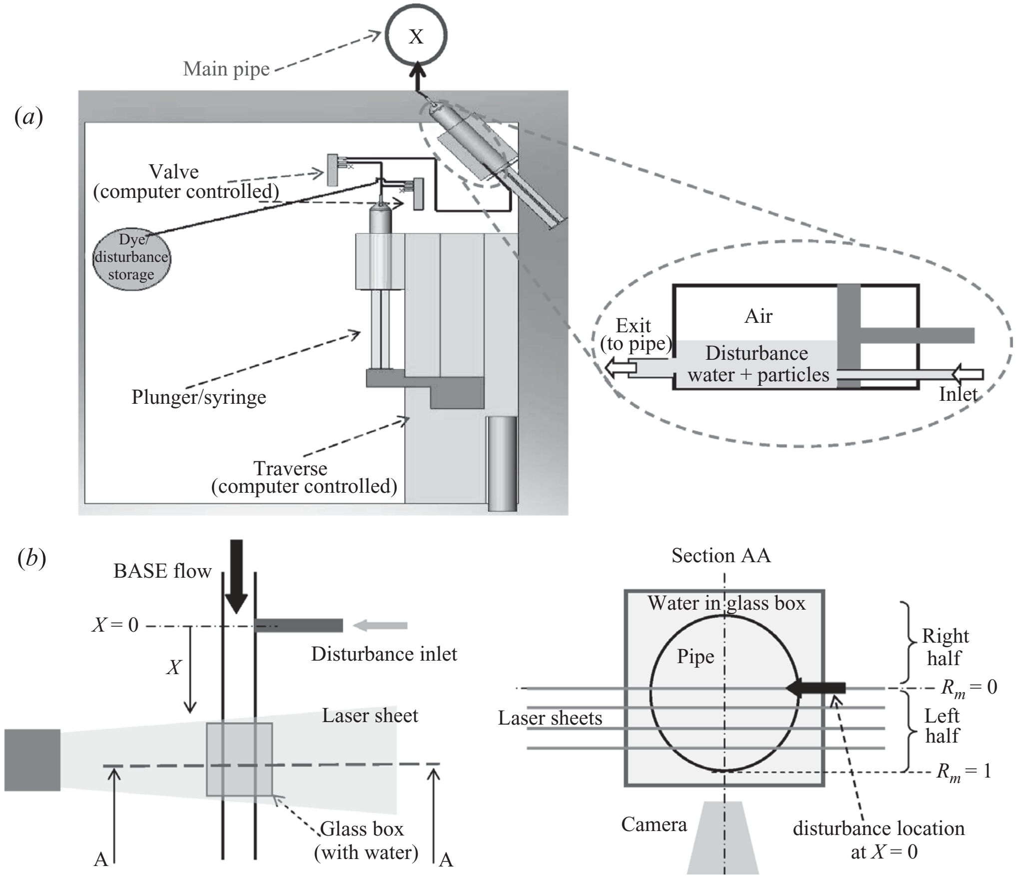

FIGURE 2. (*a*) Disturbance injection set-up used with PIV measurements. The inset shows a fluctuation damping mechanism placed just before the disturbance enters the pipe. (*b*) Schematic illustration of PIV set-up and section AA showing various planes for PIV maps.

To minimize the curvature effects of the pipe during the PIV imaging process (see figure 2*b*), a glass box filled with water, the working medium, is placed between the camera and the main pipe. All the dimensions are normalized with the radius of the pipe, R_0 and U_{cl}. The normalized axial distance, X, is positive in the downstream direction starting at the location where the disturbance is injected (figure 2*b*). PIV measurements are carried out in planes parallel to the axis of the pipe and the axis of the disturbance inlet, at different radial locations, as shown in section AA of figure 2(*b*). The laser sheet along with the camera are mounted on a micrometre scale which can be precisely positioned to get PIV maps (in the X–R plane) at various radial measurement locations (R_m), from $R_m = 0$ at the centre, to 1 at the edge of the pipe, in steps of $0.1R_0$. Since the disturbance is injected symmetrically to $R_m = 0$, the measurements are confined to the left half of the pipe cross-section relative to the injection (see figure 2*b*, section AA). The velocity maps are time averaged over 40 different realizations obtained at a sampling frequency of 15 Hz (which depending upon Re roughly translates to the crossing of about 5–10 hairpins). For each R_m-location the velocity measurements from PIV are then averaged in the steamwise direction (of about 1.5 R_0) and the average is assigned to the mid X-value

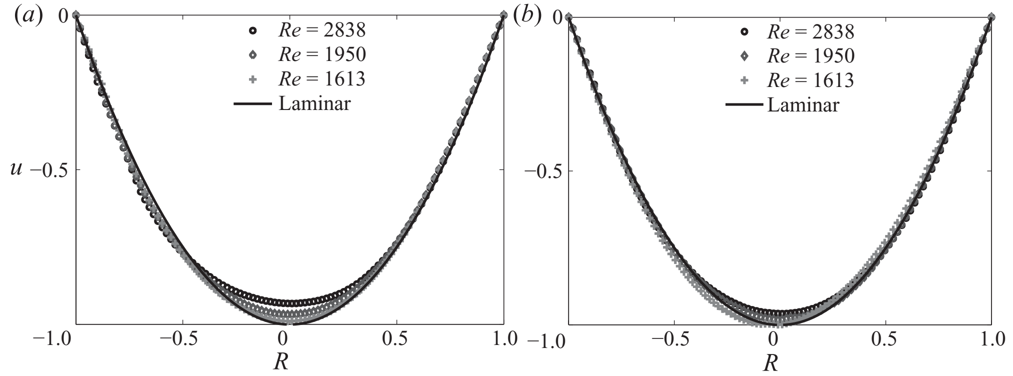

FIGURE 3. Centreline ($R_m = 0$) velocity profiles of the pipe for various Re; full line shows the equivalent profile for a laminar pipe flow. (*a*) $X = 3.7$. (*b*) $X = 85.7$.

of the plane; furthermore all the R_m-locations are stitched together (to be explained in detail later). To investigate the decay/growth of disturbances along the downstream direction, the PIV set-up is moved to various X-locations and velocity measurements are carried out. At each X-location experiments are conducted for different Reynolds numbers and injection velocities.

A note is made of the fact that, since the values of v_0 are normalized w.r.t. U_{cl}, a higher Re demands higher physical injection velocity, which beyond a certain level causes the disturbance to strike the other side of the pipe and consequently repeatable coherent structures are not possible to generate. On the other hand, lower Re and even moderate v_0 require a very low physical injection velocity which is not possible to measure with the measurement system used. All the experiments are designed under these restrictions, but were sufficiently effective for the present study, for $Re = 500$–3000.

Typical centreline ($R_m = 0$) velocity profiles of the pipe for various Re are shown in figure 3 at two extreme locations of observation, i.e. $X = 3.7$ and $X = 85.7$. The experimental velocity profiles are normalized by their equivalent laminar volume flux. There is a slight underdeveloped flow (calculated as $(U_{lam} - U_{expt})/U_{lam}$ at $R = 0$) at $Re = 2838$ and 1950 of 6.8% and 3.2 %, respectively. The results for the formation of streaks and hairpins is negligibly affected by this, because the viscous time scale is more than two orders of magnitude longer than the typical time scale of hairpin generation. To provide an approximate estimate, the viscous time scale is $R_0^2/\nu \approx 100\,\mathrm{s}$, whereas the time scale on which hairpins are developed is given by the reciprocal of their shedding frequency (a typical value of which is 2.2 Hz and is obtained from figure 15*b*). Thus the viscous time scale is ≈200 times longer than the typical time for hairpin shedding. Moreover, at the downstream location of $X = 85.7$ the underdevelopment for $Re = 2838$ is 3.7 % and for other Reynolds numbers the development is better than 2 %.

3. Results

3.1. *Critical disturbance amplitude for the generation and decay of streaks and hairpins*

Flow visualization is carried out to observe the generation of streaks and hairpin vortices in pipe flow. Water-soluble dye makes the various vortical structures visible when a continuous jet of dyed disturbance fluid is injected into the pipe flow. Some results of flow visualization are presented in figure 4. Streaks are generated for low

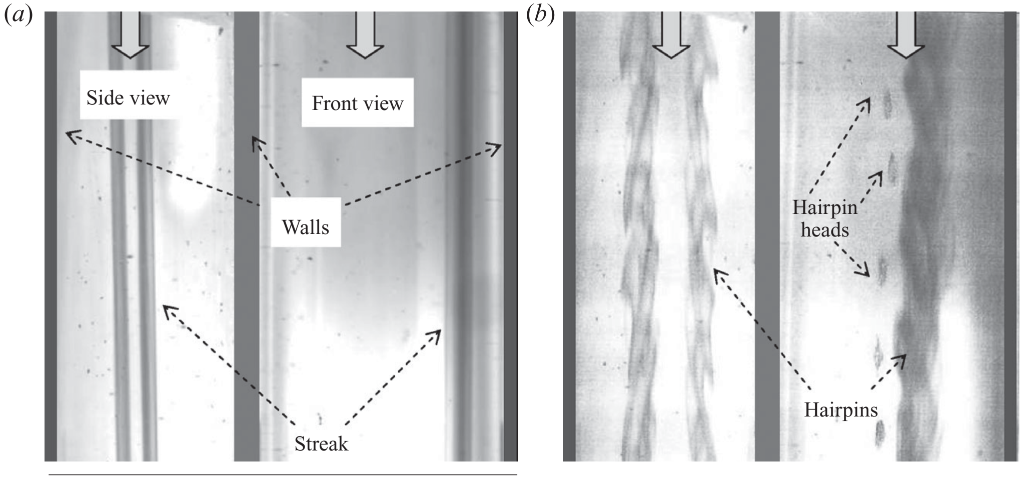

FIGURE 4. Flow visualization results at $Re = 1046$ at $X \approx 6.6$, showing two perpendicular views of coherent structures in the pipe. (*a*) Generation of streaks for low values of v_0. (*b*) Generation of hairpins for v_0 higher than the critical value.

values of injection (v_0) as photographed in figure 4(*a*) at $Re = 1046$, where the observation point (centred around $X \approx 6.6$) is close to the disturbance inlet location. It shows two simultaneously captured perpendicular views of the streaks or the CVP, which are almost streamwise independent elongated structures. Increasing v_0 beyond a critical value (depending on Re), the streaks become unstable and an array of hairpin vortices are generated, as shown in figure 4(*b*).

A detailed development of the coherent structures using flow visualization is shown in figure 5 for $Re = 1300$ while increasing v_0 (from figures 5*a* to 5*f*). It is noted here that unlike all the other flow visualization pictures presented in the present work, in figure 5, the two sides of the pipe are taken independently to obtain better focusing. For relatively low values of v_0 (figure 5*a*) the side view shows a 'single' streaky pattern and the front view shows the dyed disturbance attached very close to the pipe wall. When v_0 is increased to 0.33 (figure 5*b*) the streak becomes a 'double' legged structure and instabilities slowly emerge in the front view. For the critical value of $v_0 = 0.37$ (figure 5*c*) tiny heads of hairpins begin to appear on top of the wavy streak. Higher values of v_0 clearly enables (in the 'front view') a better visualization of the hairpins' appearance when their heads emerge out of the streaks. Figure 5(*f*) shows the typically large hairpins when v_0 is increased to a sufficiently high value.

By varying Re, the observed critical values are plotted on a log–log scale in figure 7 for $X = 6.6$. The line plotted through the observation points show a scaling law of $v_0 \sim Re^{-1}$ (Cohen, Philip & Ben-Dov 2009). Here the exponent -1 is obtained in our relatively short pipe flow facility. The same scaling law was previously obtained by Hof *et al.* (2003), indicating transition to a turbulent state in their long pipe of 785 diameters. The importance of coherent structures for the purpose of obtaining scaling laws in relatively short channels is described in Philip *et al.* (2007). The idea there is to reduce the time scales of the formation of coherent structures by increasing the injection velocity. The present work carried out in pipe flow is in the same spirit.

At a further downstream distance (from the location of injection) the hairpins are observed to decay (or disintegrate) leaving a streaky kind of structure. For $Re = 1046$ and $v_0 = 0.525$ figure 6(*a*(i)) shows the side view of hairpins at $X \approx 8$

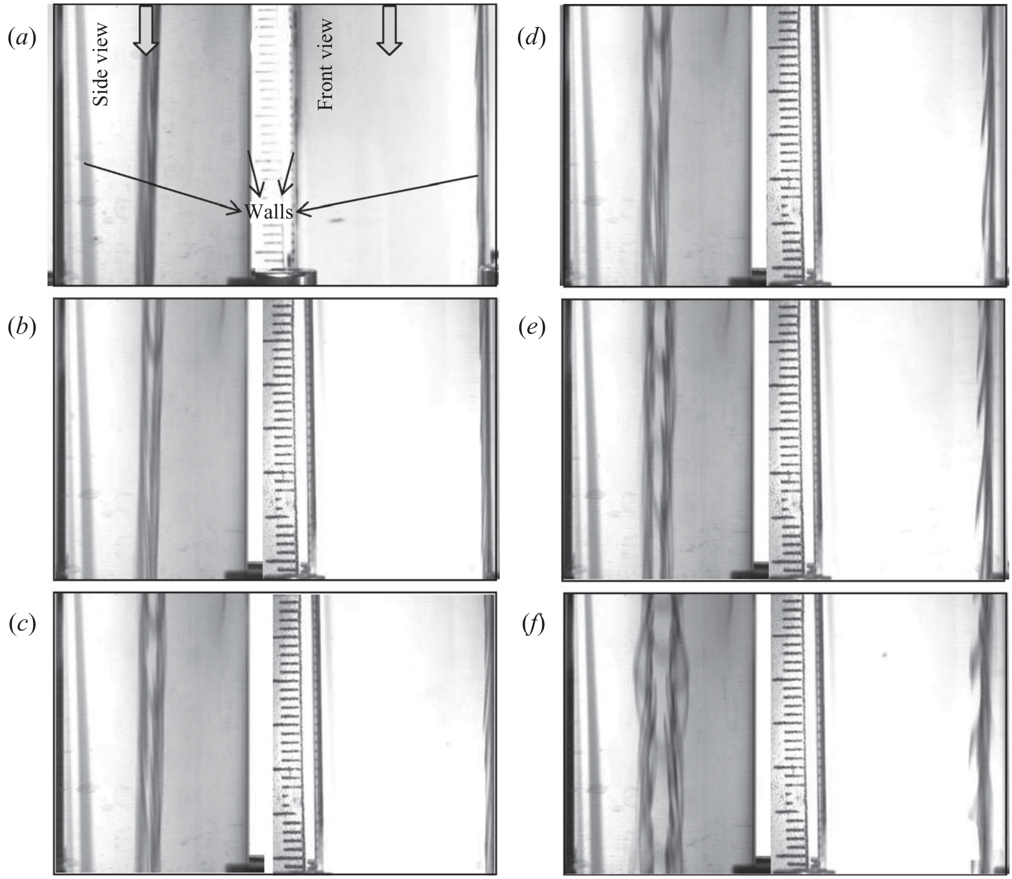

FIGURE 5. Flow visualization results at $Re = 1300$ at $X \approx 6.6$, showing two perpendicular views of coherent structures in the pipe (captured independently for better focusing, unlike figure 4). The scales shown in the photographs have gradations that are 1 mm apart. (*a*) $v_0 = 0.25$. (*b*) $v_0 = 0.33$. (*c*) $v_0 = 0.37$. (*d*) $v_0 = 0.38$. (*e*) $v_0 = 0.43$. (*f*) $v_0 = 0.56$.

and figure 6(*a*(ii)) shows the flow under the same conditions but at a downstream distance of $X \approx 46$. The hairpins are not observed downstream indicating their decay as they proceed in the flow direction. Centreline velocity profiles (at $R_m = 0$) of u, (the difference between the base flow and the flow with the disturbance for the same flow conditions) are shown in figure 6(*b*). The distribution of u for $X = 3.7$ is that of hairpin vortices. With increasing X, u vanishes, implying that the velocity profile returns back to the parabolic velocity profile of the laminar flow. The decay of hairpin vortices with increasing X points to the fact that the critical v_0 at which hairpins are first observed should vary with the downstream distance. Plotting in figure 7 the critical v_0 (for two additional X-locations) shows that, for the same Re, a higher v_0 is required when the observation point is moved downstream for the first appearance of hairpins. For a constant v_0, the spacing between the three different lines indicates that hairpins decay more slowly as the Reynolds number is increased. Each point in figure 7 is checked by conducting at least three different experiments and the average value of the observations is presented. The error bars in the figure show the experimental uncertainty encountered in the measurements of v_0 and Re. One

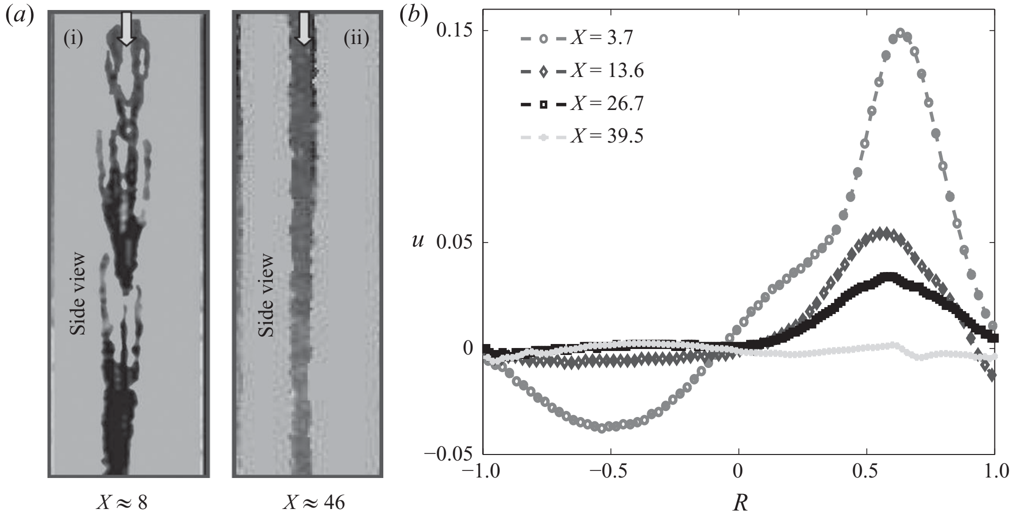

FIGURE 6. Decay of hairpins for $Re = 1046$ and $v_0 = 0.525$. (*a*) Results from flow visualization, (i) $X \approx 8$, (ii) $X \approx 46$. (*b*) Distributions of u (the difference between the base flow and the flow with the disturbance) along the centreline ($R_m = 0$) for increasing X-locations, obtained from PIV maps. The photograph in (*a*) has been reworked for clarity by removing the background noise and enhancing the coherent structures using fewer levels of grey scale.

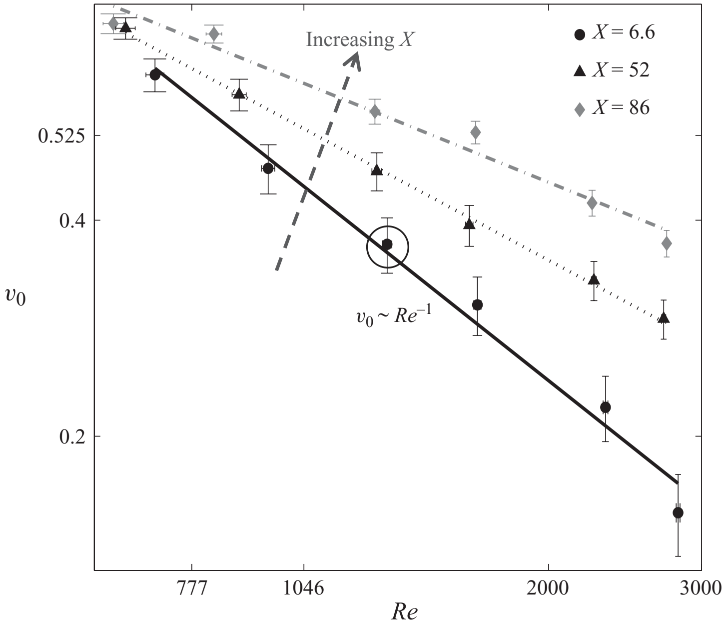

FIGURE 7. Log–log plot of v_0 versus Re for the initiation of hairpin vortices for different X-locations. The variation in the slopes shows the decay of hairpin vortices along the streamwise direction. Even though this figure is plotted on a log–log plot and suits well the present set of data, if more measurements with a broader range were used, it could not be stated conclusively that the data will still follow the logarithmic scale.

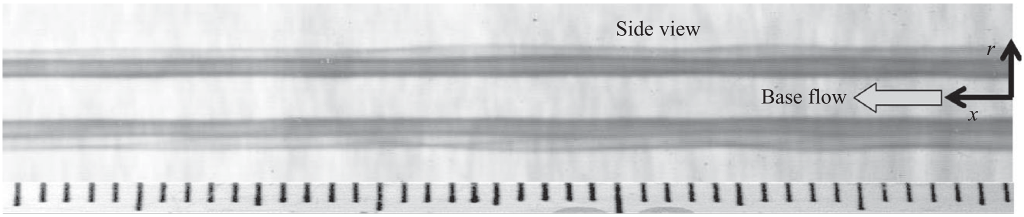

FIGURE 8. Flow visualization results at $Re = 1300$ and $v_0 = 0.37$ indicating the instability growing over the streaks. The figure shows the side view of the wavy streaks.

single point corresponding to $Re = 1300$ and the critical $v_0 = 0.37$ (shown by a circle in figure 7) has been checked more thoroughly with two different injection set-ups to confirm the validity of the measurements. The observation of critical v_0 becomes difficult when higher Reynolds numbers are approached; so the protrusion of the head of the hairpins above the base streak is observed through a video to identify critical v_0 (as seen in figure 5).

To illustrate the instability of streaks, figure 8 shows a clearer photograph of the growth of waves over streaks for a particular $Re = 1300$ and the corresponding critical injection velocity $v_0 = 0.37$. The location of this point is shown with a circle on the log–log graph of figure 7. The base flow in this figure is from right to left and the spacing between each gradation on the scale is 1 mm. The figure is the side view wherein the wavy structure of the streaks is visible. The instability observed is that of varicose type which can give rise to hairpin vortices. The determination of the critical amplitude was done through a careful examination of the videos of hairpin generation. It is noted that the amount of dye in the disturbance can also have a small effect on the observation of the initiation of hairpins; to minimize which, the smallest concentration of the dye (which is still possible to observe) has been employed. Prior to this, several preliminary visualization studies were conducted to practice the detection of the hairpin vortices and to check the dye effect. After few readings the whole closed-loop base flow is removed and refilled with fresh water, as the whole water system becomes coloured, making the detection of the hairpins difficult.

3.2. *Transient growth of energy and its decay along the streamwise direction*

To explain the deduction of disturbance velocity and vorticity maps in the R–θ plane, and the disturbance energy (to be defined later) at a particular X-location from several PIV maps obtained at various R_m-locations (see figure 2*b*), the processing of data is presented for a particular case (with $Re = 2838$ and $v_0 = 0.525$). Later, the same process will be applied to various Reynolds numbers and v_0 at various X-locations for the presentation of comparative results.

Figure 9 shows velocity maps obtained at $Re = 2838$ at $X = 3.7$ (the closest axial location to the disturbance injection) for $v_0 = 0.525$. This is the highest Re used in this study and therefore, corresponds to the least fully developed base flow. Figure 9(*a*–*d*) presents results for four different R_m-locations with each one of them averaged over 40 realizations. Figure 9(*a*(i)–*d*(i)) (the top row) shows the corresponding laminar velocity profile (for the same volume flux), the base flow (without disturbance, v_0) and the flow with v_0. (Note that the measured velocities are shown in the downwards, negative direction, corresponding to the direction of the flow in the experimental set-up.)

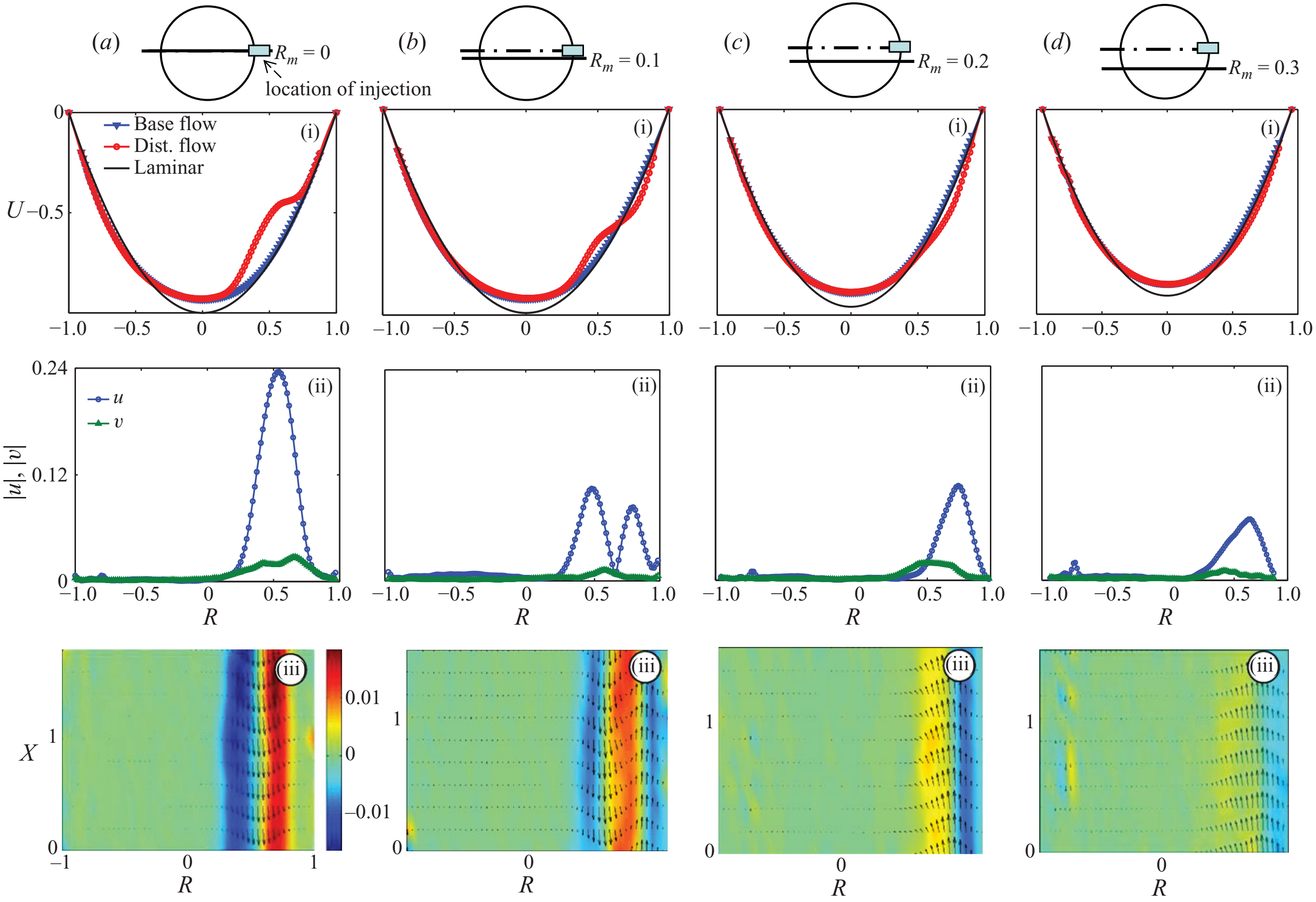

FIGURE 9. PIV results for $Re = 2838$, $v_0 = 0.525$ and $X = 3.7$. (*a*) $R_m = 0$, (*b*) $R_m = 0.1$, (*c*) $R_m = 0.2$ and (*d*) $R_m = 0.3$, (i) averaged base flow, disturbance and analytical velocity profiles, (ii) absolute values of disturbance velocity, (iii) maps of (u, v), shaded by vorticity in the measurement plane.

Figure 9(a(ii)–d(ii)) (the middle row) presents the magnitude of the disturbance velocity (the difference between the base flow and the flow with the disturbance, u - axial, v - perpendicular to u in the plane). Figure 9(a(iii)–d(iii)) (the bottom row) shows the disturbance PIV map (with shades showing the associated disturbance vorticity, $\partial u/\partial R - \partial v/\partial X$, in the measurement plane).

The velocity profiles are obtained by averaging the PIV map that is about 1.5 in the X-direction (small compared to the separation distance between two consecutive axial measurement points which varies between 10 and 46). Increasing R_m (i.e. coming closer to the wall), figure 9 shows that the total base flow velocity decreases (observed by the decreasing magnitude of U), and the effect of the disturbance also diminishes (which can be observed by the decreasing magnitudes of u and the fading of vorticity in the vector maps). The vector maps are restricted to R_m-locations where the disturbance field is still significant (which is also a function of Re, v_0 and X-location). In this example velocity measurements are carried out at four R_m-locations. It should be emphasized here that the number of R_m-locations in each experiment is a variable and it is decided such as to capture the disturbance fully at each X-location. The influence of the disturbance in the R–θ plane is felt (as observed in the PIV image) in the pipe to varying degrees, depending primarily on v_0 and X-location and to a lesser degree on Re. So each time an experiment is started, the plane $R_m = 0$ is first captured, and then the R_m is increased in steps of $0.1R_0$ (as mentioned above), till that R_m where the disturbance is no longer affecting the flow. To give some examples, in figures 9 and 10 there are four R_m-locations, but there are eight in figure 11(c(4d)), and seven R_m-locations in figure 11(c(4e)).

Once the axial disturbance velocity at all R_m-locations is obtained, they are stitched together with the aid of interpolation to get a map of u, at a particular X-location. The data of u from figure 9(a(ii)–d(ii)) are plotted in figure 10(a(i)), with blue and red corresponding to regions where the velocity of flow with the disturbance is higher and lower, respectively, than the base flow. The data are then extrapolated (assuming that u vanishes in $0.2R_0$ from the last R_m-location where the data are obtained) and reflected (since the disturbance is symmetrically injected), to obtain a map for u in the whole R–θ plane, as presented in figure 10(a(ii)). The energy (defined in (3.1)) is calculated by two methods; one, by the measured data and, second, by extrapolating those values of u. Any error involved in this extrapolation is less than the size of the symbols used to present the data in figures 11(a) and 13. Forming a local two-dimensional coordinate system, x_1 and x_2 (as shown in figure 10a(ii)), an in-plane vorticity, $\omega_{x_1x_2}$ (e.g. van Doorne & Westerweel 2009) can be defined as the first expression in (3.1). In the present case, it represents the averaged projection of the coherent structure (streak or hairpin) onto a single R–θ plane. The distribution of $\omega_{x_1x_2}$ shows the variation of the averaged axial disturbance velocity formed by the coherent structure (over an axial distance of about $1.5\,R_0$,) projected in the R–θ plane. Furthermore a norm indicating the strength of the disturbance is taken as the energy, $E(X)$. Both $\omega_{x_1x_2}$ and $E(X)$ are defined as

$$\omega_{x_1x_2} = \sqrt{\left(\frac{\partial u}{\partial x_1}\right)^2 + \left(\frac{\partial u}{\partial x_2}\right)^2} \qquad \text{and} \qquad E(X) = \int_0^{2\pi}\int_0^1 u^2\, r\,\mathrm{d}r\,\mathrm{d}\theta. \tag{3.1}$$

For example, the energy ($E(X = 3.7)$) for the disturbance in figure 10(a(ii)) is 1.23×10^{-3}, which is approximately 1.2 % of the base flow energy. The contours of $\omega_{x_1x_2}$ are plotted in figure 10(b).

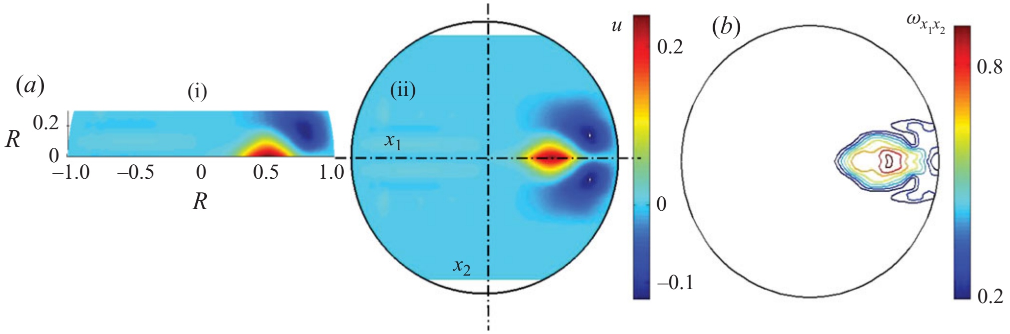

FIGURE 10. Plots of u and $\omega_{x_1x_2}$ from the data of figure 9. (*a*) u plot by stitching the data at different values of R, (i) measured velocity profiles (with in-between values interpolated), (ii) extrapolated values of u in the R–θ plane. (*b*) Contours of $\omega_{x_1x_2}$.

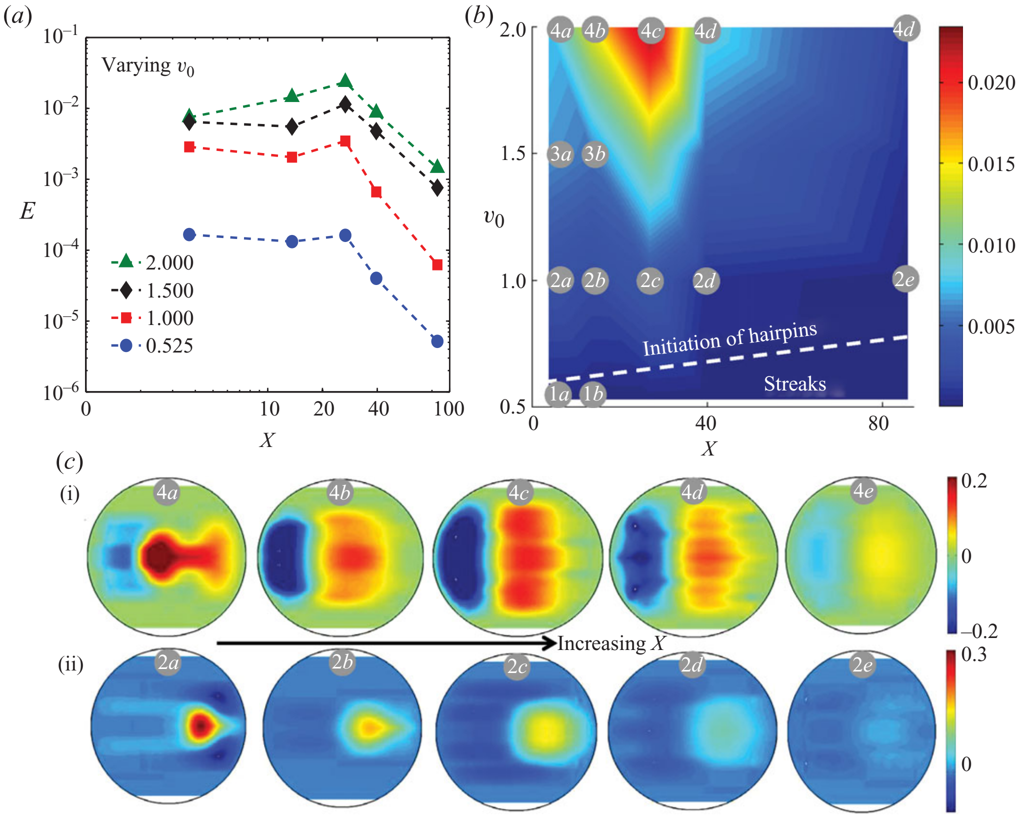

FIGURE 11. Development of disturbance in the axial direction for $Re = 777$. (*a*) log–log plot of the variation of energy along the steamwise direction for varying v_0. (*b*) Same data as (*a*) but on a flooded plot of energy on a v_0 versus X plane. (*c*) Variation of u in X-direction, (i) $v_0 = 2.0$, (ii) $v_0 = 1.0$.

Figure 11 shows the development of the disturbance in the axial direction for $Re = 777$ and various v_0. PIV measurements are performed at five different X-locations, corresponding to $X = 3.7$, 13.6, 26.7, 39.5 and 85.7. Figure 11(*a*) is an E versus X log–log plot for four different v_0, where, for each v_0, the energy increases transiently and then there is a sharp decay, with approximately the same decay rates. The same data

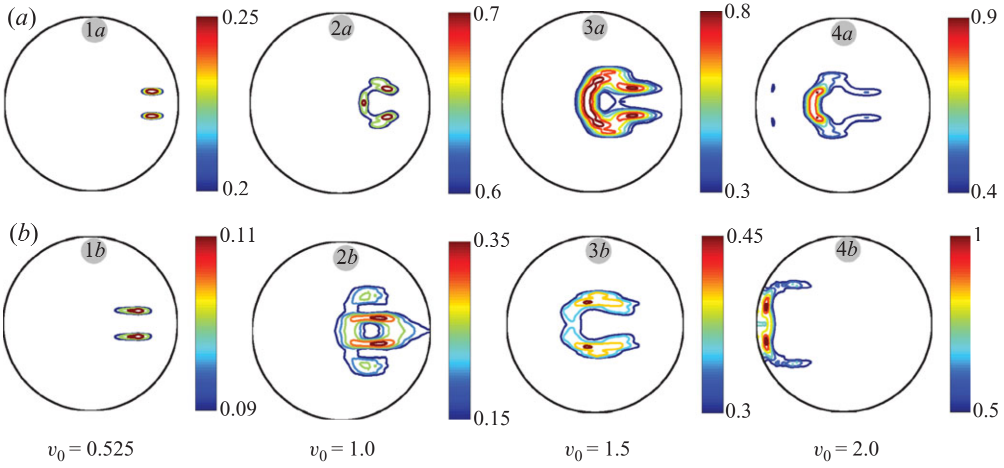

FIGURE 12. Contours of $\omega_{x_1x_2}$ for $Re = 777$. (*a*) $X = 3.7$ (closest to the location of injection). (*b*) $X = 13.6$.

are shown in a different form in figure 11(*b*), where filled-contour map of energy is presented (in colour) on a v_0 versus X plot. For convenience various regions in the map are labelled from 1 to 4 and (*a* to *e*) indicating v_0 and X-location of measurements, respectively. Figure 11(*c*) plots u for two v_0; $v_0 = 2.0$ (top row) and $v_0 = 1.0$ (bottom row), at five different X, labelled from 4*a* to 4*e* and 2*a* to 2*e*, respectively, in correspondence with the labels in figure 11(*b*). The difference in the way the disturbance evolves in both cases can be seen distinctly; for $v_0 = 2.0$, increase in energy is attributed to the increases in the magnitude of disturbance as well as the region in the R–θ plane where the influence of the disturbance is felt, also referred to here as the area of influence (AoI), and the decay is due to decrease in the magnitude. On the contrary, for $v_0 = 1.0$, the magnitude of the disturbance is continuously decreasing while any initial increase in energy is due to the increase in the AoI and the decay is due to approximately constant AoI (figure 11*c*(2*c*–*e*)) and decreasing magnitude.

In figure 11(*b*) the (white) demarcating dashed line (plotted from the data of figure 7 for $Re = 777$) shows approximately the conditions where the hairpins appear for the first time, based on the flow visualization results. In figure 7, at $Re = 777$, a vertical line will cut three X lines (corresponding to three X-locations) at three points corresponding to three values of v_0. These three values (of X, v_0) are plotted in figure 11(*b*) and a line is drawn through them. The region below the line contains only streaks and above it hairpins and other nonlinear processes appear. The line can be interpreted as the boundary separating the linear and the nonlinear processes. To further clarify the boundary and as a quantitative confirmation of the flow visualization, figures 12(*a*) and 12(*b*) show the contours of $\omega_{x_1x_2}$ at X-locations *a* and *b*, respectively, for increasing v_0. For a low injection velocity, in figure 12(*a*(1*a*)) the contours show the streamwise vortices (from the accompanying streaks). As the downstream distance is increased the vortices move towards the centre and stretch, as observed in figure 12(*b*(1*b*)). Increasing v_0 produces hairpin vortices of higher strength which move closer to the other side of the wall. A similar effect is observed when X is increased. It can be noticed that for the highest v_0, the hairpin appears immediately at the centre of the pipe (figure 12*a*(4*a*)) and moving further downstream causes the hairpin to hit the opposite side of the wall (figure 12*b*(4*b*)). The observation of streamwise vortices (or streaks) and hairpins from the vorticity contours are in

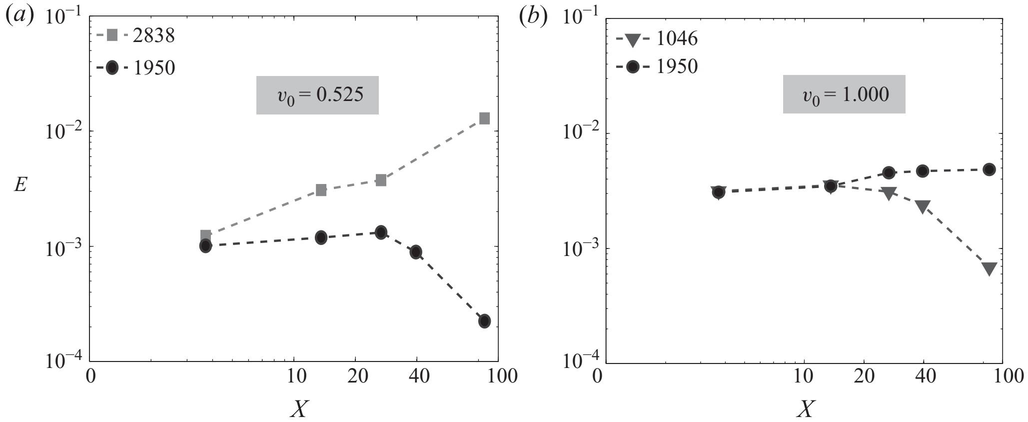

FIGURE 13. Variation of E along X on a log–log plot. (*a*) $v_0 = 0.525$ and $Re = 2835$ and 1950. (*b*) $v_0 = 1.0$ and $Re = 1950$ and 1046.

accordance with those found by flow visualization, and depicted by the dashed line in figure 11(*b*). No clear coherent structures are found for higher v_0 because the form of the disturbance is destroyed by the disturbance hitting the other side of the wall, and also with increasing downstream location they lose their coherence. Therefore the structures are difficult to be captured in the averaged vorticity contours.

The evolution of the disturbance for higher Re is presented next. Figure 13(*a*) shows on a log–log graph the evolution of energy for $Re = 2838$ and 1950 for $v_0 = 0.525$. For $Re = 1950$, the energy increases for some downstream distance but then decays, whereas for $Re = 2838$, the disturbance continues to increase and does not decay in the limited axial distance of measurements presented here. Based on visual observation, it seems that at this high Re, the disturbance does not decay downstream but continues to increase to make the flow completely turbulent further downstream. For a higher $v_0 = 1.0$, in figure 13(*b*), energy for $Re = 1950$ does not decay, unlike $v_0 = 0.525$. The experiments for a lower $Re = 1046$ show the usual transient increase and further decay of energy. Figure 14 shows the structure of u in the R–θ plane corresponding to the energy plots in figure 13. Figures 14(*a*) and 14(*b*) present the evolution of the disturbance at $v_0 = 0.525$, for $Re = 2838$ and $Re = 1950$, respectively. For $Re = 2838$, the disturbance increases in both magnitude and area with increasing X, and consequently the energy also increases, whereas for $Re = 1950$, the energy decreases as a result of the decreasing magnitude of u. The initial amplitude ($v_0 = 0.525$) at $Re = 2838$ is large enough for the disturbance to increase continuously in the present experiment, unlike for the case of $Re = 1950$. However, for $v_0 = 1.0$ and $Re = 1950$, figure 14(*c*) shows the increase in area occupied by u (or an increase in AoI) resulting in the increase in E, even though the magnitude of u is decreasing with X. And for $Re = 1046$ and $v_0 = 1.0$, as shown in figure 14(*d*), u decays and subsequently the energy also decays (even though E increases transiently due to increasing AoI). Thus, it can be concluded that the energy of the disturbance is a function of both the amplitude of disturbance and the area of influence.

4. Discussion

Transient growth has proved quite successful in providing a growth mechanism where linear mode analysis fails to predict instability. The disturbance that grows

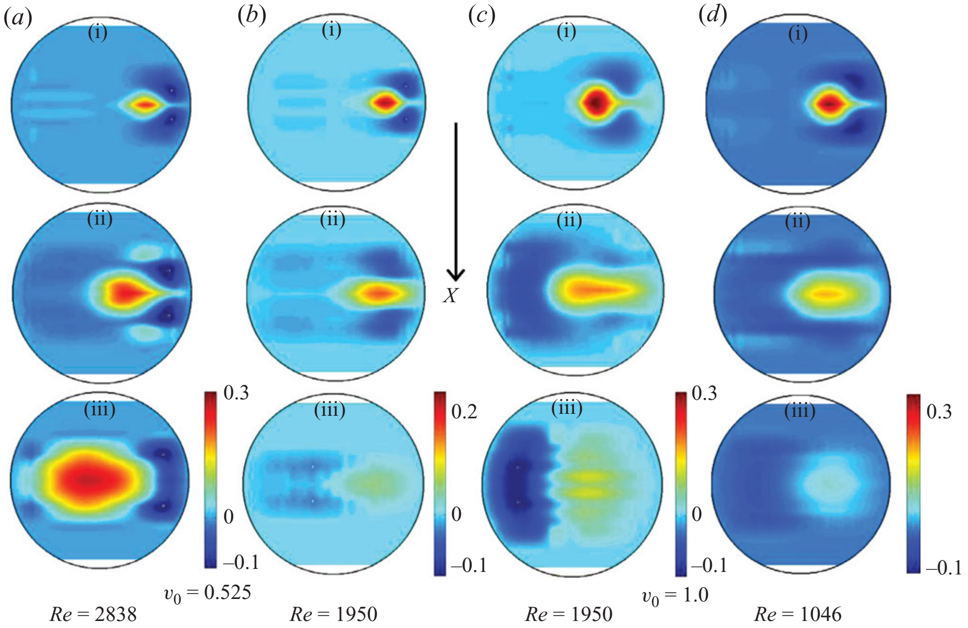

FIGURE 14. Variation of u along X. (a) $Re = 2838$, $v_0 = 0.525$, (b) $Re = 1950$, $v_0 = 0.525$, (c) $Re = 1950$, $v_0 = 1.0$ and (d) $Re = 1046$, $v_0 = 1.0$; (i) $X = 3.7$, (ii) $X = 26.7$, (iii) $X = 85.7$.

the most includes a combination of many normal modes and has been found to be streamwise independent vortices forming streaks (Schmid & Henningson 1994). The same mechanism can also be explained by considering two least stable modes of pipe flow (Ben-Dov *et al.* 2003; Cohen *et al.* 2009). The existence of such structures in pipe flow is demonstrated here. However, as seen in figure 11(a) for $v_0 = 0.525$, streamwise vortices (or streaks) are not extended infinitely in the streamwise direction, which is the usual assumption in theoretical considerations, instead they decay downstream in about 10–15 diameters. However, compared to the core diameter of the CVPs, their length is about two orders of magnitude greater.

Both flow visualization and velocity measurements show that for a particular Re and X-location for small values of v_0, streaks (or counter-rotating vortices) are formed and beyond a critical v_0 when streaks become stronger, hairpin vortices are generated (e.g. figure 4). Observations show that on increasing v_0, the streaks become wavy and from the crest of these waves, an array of hairpins appears (e.g. figure 8). It is also observed that the velocity profiles of the flow with the disturbance are inflectional, suggesting the possibility of an instability. To check this, stability analysis is performed based on two centreline velocity profiles at $Re = 777$ and 1046 for $v_0 = 0.525$, shown in figure 15(a), for $X = 3.7$. It can be seen from figure 7, that for $Re = 777$ and $v_0 = 0.525$, only stable streaks are observed and whereas at $Re = 1046$, v_0 is just sufficient to produce hairpins. Spatial linear stability equations (Orr–Sommerfeld and Squire) for the two base flow velocity profiles are solved using a spectral method employing 120 Chebychev polynomials, assuming a variation in the base flow profiles only in the radial coordinate. The results show the existence of unstable modes for $Re = 1046$ and stable ones for 777. The growth rate ($-\alpha_i$) versus frequency in dimensional values is plotted in figure 15(b). The most unstable wave for $Re = 1046$

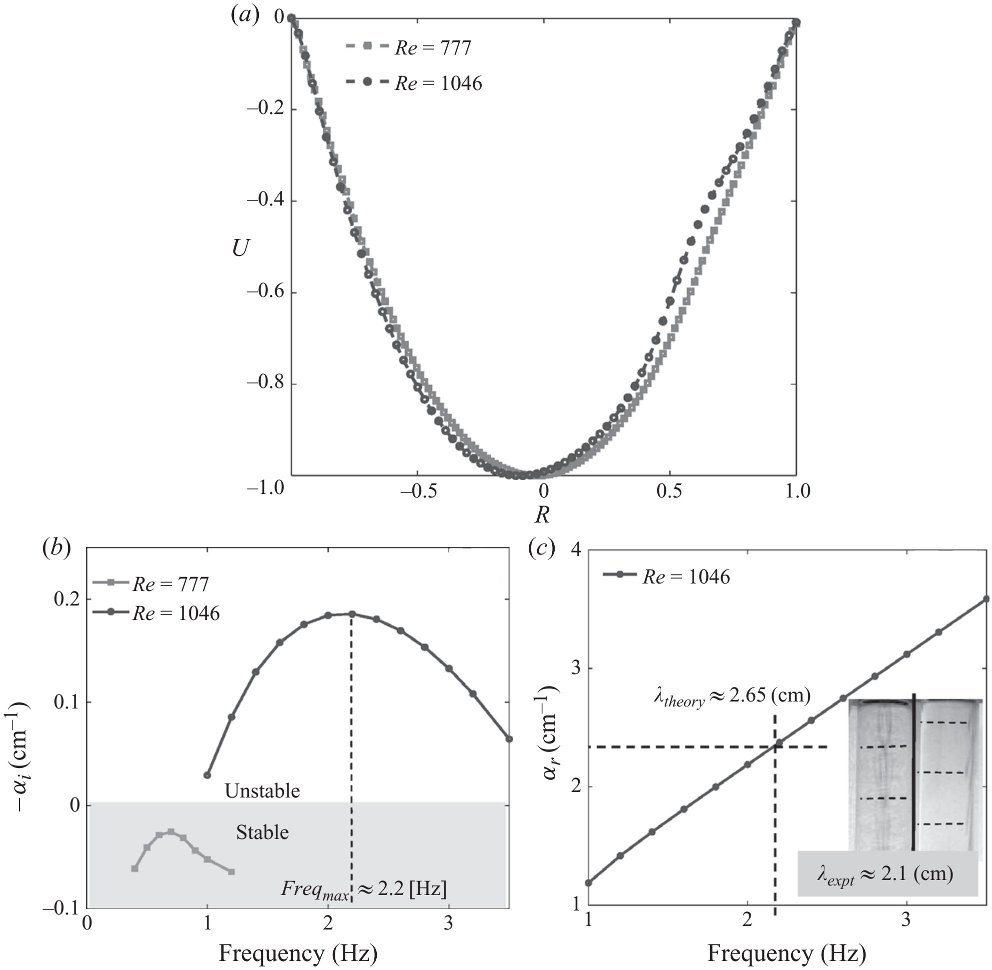

FIGURE 15. Stability for $v_0 = 0.525$ and $X = 3.7$ at $Re = 1046$ and 777. (*a*) Velocity profiles at $R = 0$. (*b*) Growth rate ($-\alpha_i$) versus frequency curve. (*c*) Wavenumber (α_r) versus frequency curve for $Re = 1046$.

has a frequency of 2.2 Hz and has an associated wavelength (α_r in figure 15*c*) of 2.65 cm. The measured wavelength in the experiment is about 2.1 cm (see the inset in figure 15*c* which is based on figure 6*a*(i)). The closeness of the observed and predicted values (even when the assumptions of a parallel and two-dimensional flow are not fully justified) shows that the inflectional instability particularly dominates the wavelength selection during the formation of hairpins.

The numerical study by Zikanov (1996) of temporal secondary instability of streaks by three-dimensional perturbations shows transient growth and decay of energy for small streak amplitudes and a continuous increase for larger amplitudes. This is in accordance with the results presented here. Transition to turbulence in pipe flow has also been observed to be associated with the secondary instability of streaks (Meseguer 2003). The phenomenon of streak generation and their breakdown due to secondary instability is quite general and is found in other flows too, where subcritical transition takes place, for example, in boundary layer flows (e.g. Matsubara & Alfredsson 2001;

Schlatter *et al.* 2008) and in plane channel flow (e.g. Elofsson & Alfredsson 1998; Philip *et al.* 2007).

It is interesting to note that the streaks and hairpins are generated in a similar manner by Svizher & Cohen (2006) and Philip *et al.* (2007) in channel flows. They, however, have not observed any decay of the streaks or hairpins along the streamwise direction (see for example, Svizher & Cohen 2006, figure 6). This difference between the channel and pipe flow is probably due to the confining effects of the wall in a pipe which is absent in a two-dimensional channel. It is also noted that there is a fairly large body of studies related to the jet-in-cross-flow (e.g. Fric & Roshko 1994; Bagheri *et al.* 2009 and references therein), though not in pipe flow that we know of. The emphasis in these studies are mainly on higher values of v_0 which give rise to more complicated structures than streaks and hairpin vortices. It is also worth mentioning the study by Sau & Mahesh (2008) wherein a numerical simulation for a low v_0 (or jet-to-cross-flow velocity ratio) gives rise to the shedding of hairpin vortices in a laminar boundary layer.

Streaks are generated via a linear process whereas the generation of hairpin vortices is a nonlinear process, initiated by the breakdown of these streaks due to secondary instability. Hairpin vortices are three-dimensional rotational and induce high mixing in the flow (relative to molecular diffusion). All the characteristics that represent hairpins (observed in relatively laminar base flows, like in the present experiments) also apply to a regular turbulent flow. Hairpins that are found in fully turbulent flow are believed to be the main coherent structure that gives turbulence its characteristic form. It has been also found (Cohen *et al.* 2009) that the scaling of $v_0 \sim Re^{-1}$ is required to cross from the linear regime with streaks to the nonlinear one with hairpins (for small X-locations). This is the same scaling as observed in the 'real' transition of laminar state to turbulent in pipe flow by Hof *et al.* (2003), showing that the Re at which turbulence is generated is a function of the amplitude of the disturbance, $\mathscr{D}$. In the present paper the amplitude of the disturbance is denoted by v_0, but, can also be taken as $E(0)$, like in many theoretical/numerical works.

As presented in the previous section, both streaks and hairpin vortices may decay downstream depending upon the values of v_0, X and Re, showing that the scaling of $v_0 \sim Re^{-1}$ varies downstream. Recently, it has been observed that turbulence in pipe flow has a tendency to decay (e.g. Hof *et al.* 2006; Peixinho & Mullin 2006). Once the turbulence is generated, it seems to decay along the length of the pipe. This points to the fact that apart from the already existing parameters of Re and disturbance amplitude $\mathscr{D}$ on which the transition to turbulence in pipes depends, another relevant parameter is $\mathscr{L}$. Here, $\mathscr{L}$ is the length of the pipe in which the flow remains turbulent starting from the location of perturbation (or the equivalent time) and beyond which the flow is laminar. The many similarities that have been observed between the linear–nonlinear transition (in the present work) and laminar–turbulent transition compel one to present graphically the stability diagram of laminar–turbulent transition drawing ideas based on the data of the present work and other studies on laminar–turbulent transition.

Decay of streaks and hairpin vortices along the downstream direction (shown in figure 7) depends upon the values of v_0, X and Re. The fit of data presented in figure 7 is plotted again in figure 16 (shown by three dark lines, and in-between values interpolated) on a three-dimensional coordinate system, with v_0, X and Re as the three axes. The surface demarcates the linear and nonlinear processes. It is noted that the volume under that linear regime increases with streamwise location as an indicator of the decaying hairpins.

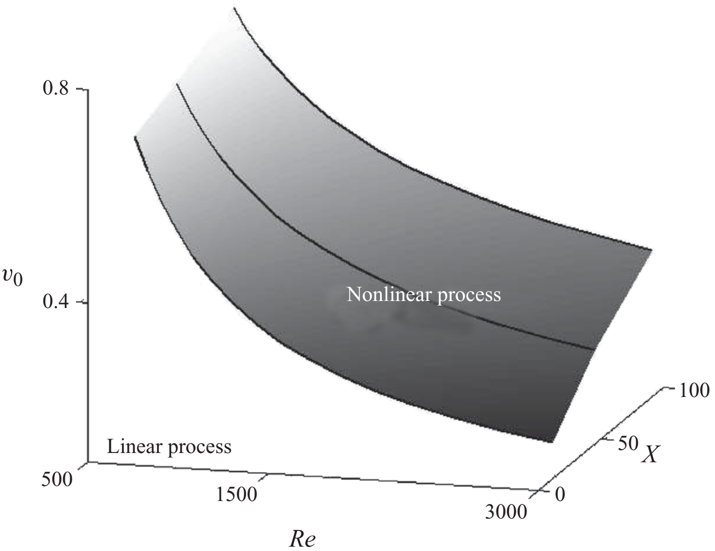

FIGURE 16. Three-dimensional transition curves in disturbance, Re and streamwise distance space. Based on flow visualization, it distinguishes the linear process (streaks) and the beginning of the nonlinear process (hairpins).

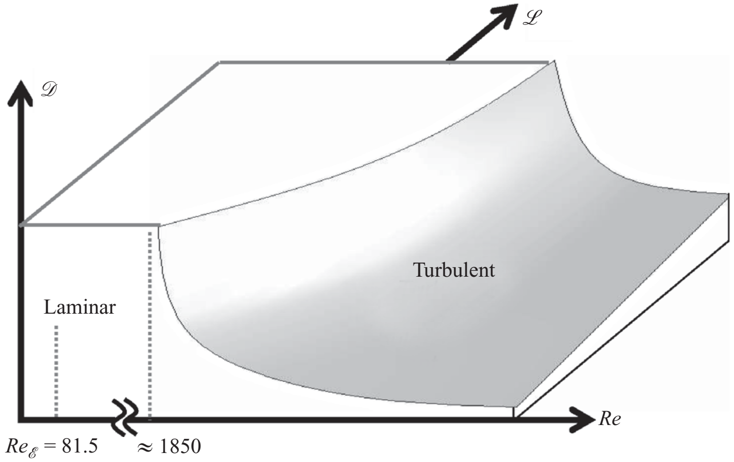

FIGURE 17. Three-dimensional transition curves in disturbance, Re and streamwise distance space. Schematic illustration of a general stability diagram for pipe flow. $Re_{\mathscr{E}}$ is the Reynolds number below which the energy of the disturbance decreases monotonically (Joseph 1976), and it is also the lower limit found by transient growth analysis (Schmid & Henningson 1994).

Based on the laminar–turbulent transition studies and the present work, a schematic diagram of pipe-transition surface is presented in figure 17, where the 'solid' region represents the laminar state and the remaining, turbulent. It can be seen that for $\mathscr{L}$ (or X)= 0, the figure recovers the usual stability diagram (e.g. Joseph 1976, p. 9). For higher values of $\mathscr{D}$ (i.e. values of $\mathscr{D}$ corresponding to $\mathscr{L} = 0$ and in the proximity of, but greater than $Re \approx 1850$), the variations in the $\mathscr{L}$–Re planes due to changes in $\mathscr{D}$ are negligible. This is in accordance with the recent studies (e.g. de Lozar & Hof 2009) where it has been shown that lifetimes of puffs (here represented as an equivalent $\mathscr{L}$), when plotted against Re, are independent of the perturbation amplitude ($\mathscr{D}$). Moreover, to draw the schematic diagram in figure 17, the understanding of the linear stage as the representative of the laminar state and the beginning of nonlinearity (marked by the initiation of hairpins) as the beginning of the turbulent state is also employed. The similarity of the surfaces presented in figures 16 and 17 is noted. With increasing $\mathscr{L}$ (or X), the domain of laminar flows (in figure 17) or the linear regime of streaks (in figure 16) increases, and consequently that of turbulence or that of the nonlinear effects along with the hairpin vortices decreases. Even though there is necessarily no direct relation between our present findings (of transition from linear to nonlinear states in pipe flow) and the pipe flow transition itself, the phenomenological similarity between the two types of outlook is clear.

A point to be noted is that transition to turbulence in pipes has been found to be sensitive to the initial conditions (e.g. Brosa 1989; Darbyshire & Mullin 1995; Faisst & Eckhardt 2004), therefore statistical tools have been employed for the analysis of the data. In the present study, however, the disturbance is produced continuously (rather than intermittently, as normally done to produce puffs of turbulent flows) in a predominantly laminar flow. This ensures in the present study that streaks and hairpins vortices that are produced are indeed repeatable. Moreover, to justify the quasi-steady measurements along the axial direction in this study, it is mentioned that, since the experiments have an almost steady flow (or time periodic when hairpins are generated), the dependence is only spatial.

5. Summary and conclusions

Continuous disturbances are introduced into pipe flow producing two coherent structures, commonly found in transitional and turbulent boundary layers: streaks (accompanied by counter-rotating vortices) and hairpin vortices. The former is a well-known structure resulting from the linear process and the latter is a manifestation of nonlinear processes. Flow visualization and PIV measurements are carried out for various Reynolds numbers, amplitudes of disturbance and at various streamwise locations, allowing the study of the formation and the subsequent evolution of the coherent structures.

For all Reynolds numbers, streaks with high- and low-velocity regions are formed for low levels of disturbance amplitude. An increase in the initial amplitude causes the instability of the streaks and further breakdown into an array of hairpin vortices. It is also shown here that the combined pipe Poiseuille flow and streak velocity profile is unstable and produces wavy structure, the wavelength of which can be fairly well predicted by a simple stability analysis. Furthermore, from the crests of these waves the hairpins first appear. Scaling of critical amplitude of disturbance, v_0, for the initiation of hairpins and Re, follows $v_0 \sim Re^{-1}$ (Cohen *et al.* 2009), for the observation point very close to the injection of the disturbance. However, streaks and hairpins are found to be decaying in the streamwise direction once they are generated in the pipe flow, and thus correspond to varying decay laws for different downstream distances. Moreover, the hairpins have been found to decay more slowly with increasing Re. Velocity measurements and the subsequent in-plane vorticity in the R–θ plane confirm the existence and evolution of the coherent structures observed in the flow visualizations.

The amplitude of the disturbance is measured at various downstream distances and cross-sectional energy is evaluated. In all cases studied, the energy always increases initially and later it can decrease, except for high v_0 and Re (e.g. for $Re = 2835$ and 1950, and the value of $v_0 = 0.525$ and 1.0, respectively). The transient energy growth at any X-location depends upon the values of v_0 and Re; for higher v_0 or/and higher Re there is a higher energy growth (e.g. figure 11*a*, $v_0 = 2$; figures 13*a* ($Re = 2838$) and 13*b* ($Re = 1950$)), whereas for lower values of v_0 or/and Re, the growth is lower (e.g. figure 11*a*, $v_0 = 1, 0.525$; figures 13*a* ($Re = 1950$) and 13*b* ($Re = 1046$)). The disturbance while propagating downstream spreads in the R–θ plane and consequently the associated energy of the disturbance, which has contributions both from the area of influence of the disturbance at each cross-section and its magnitude, continues to change. Both contributions have been found to be of importance in the study carried out.

Finally, the surface which forms the boundary in the v_0, Re, X-space, separating the linear process and the nonlinear ones has a close connection with a boundary that one would expect to see between the laminar and the turbulent states of motion in pipe flow. Even though the recent research activities concerning the decay of turbulence have been of great importance, much of the boundary, presented schematically in figure 17 is yet to be revealed.

This research has been supported by the Israeli Science Foundation under Grant no. 1247/06. The authors are grateful to Efim Shulman and Oleg Kan for their help in constructing the apparatus and *LabView* programming.

REFERENCES

Bagheri, S., Schlatter, P., Schmid, P. J. & Henningson, D. S. 2009 Global stability of a jet in crossflow. *J. Fluid Mech.* **624**, 33–44.

Ben-Dov, G., Levinski, V. & Cohen, J. 2003 On the mechanism of optimal disturbances: The role of a pair of nearly parallel modes. *Phys. Fluids* **15** (7), 1961–1972.

Brosa, T. 1989 Turbulence without strange attractor. *J. Stat. Phys.* **55**, 1303–1312.

Cohen, J., Philip, J. & Ben-Dov, G. 2009 Aspects of linear and nonlinear instabilities leading to transition in pipe and channel flows. *Phil. Trans. R. Soc.* A **367**, 509–527.

Darbyshire, A. G. & Mullin, T. 1995 Transition to turbulence in constant-mass-flux pipe flow. *J. Fluid Mech.* **289**, 83–114.

van Doorne, C. W. H. & Westerweel, J. 2009 The flow structure of puff. *Phil. Trans. R. Soc.* A **367**, 489–507.

Eckhardt, B. (Ed.) 2009 Turbulence Transition in Pipe Flow: 125th Anniversary of the Publication of Reynolds' paper, 1888. In *Phil. Trans. R. Soc.* A, vol. 367.

Eckhardt, B., Schneider, T. M., Hof, B. & Westerweel, J. 2007 Turbulence transition in pipe flow. *Annu. Rev. Fluid Mech.* **39**, 447–468.

Elofsson, P. A. & Alfredsson, P. H. 1998 An experimental study of oblique transition in plane poiseuille flow. *J. Fluid Mech.* **358**, 177–202.

Faisst, H. & Eckhardt, B. 2004 Sensitive dependence of initial conditions in transition to turbulence in pipe flow. *J. Fluid Mech.* **504**, 343–352.

Fric, T. F. & Roshko, A. 1994 Vortical structure in the wake of a transverse jet. *J. Fluid Mech.* **279**, 1–47.

Guala, M., Hommema, S. E. & Adrian, R. J. 2006 Large-scale and very-large-scale motions in turbulent pipe flow. *J. Fluid Mech.* **554**, 521–542.

Hof, B., van Doorne, C. W. H., Westerweel, J., Nieuwstadt, F. T. M., Faisst, H., Eckhardt, B., Wedin, H., Kerswell, R. R. & Waleffe, F. 2004 Experimental observations of nonlinear travelling waves in turbulent pipe flow. *Science* **305**, 1594–1598.

Hof, B., Juel, A. & Mullin, T. 2003 Scaling of the turbulent transition threshold in a pipe. *Phys. Rev. Lett.* **91** (24), 2445021–4.

Hof, B., Westerweel, J., Schneider, T. M. & Eckhardt, B. 2006 Finite lifetime of turbulence in shear flows. *Nature* **443**, 59–62.

Joseph, D. D. 1976 *Stability of Fluid Motions I*. Springer-Verlag.

Kline, S. J., Reynolds, W. C., Schraub, F. A. & Runstadler, P. W. 1967 The structure of turbulent boundary layers. *J. Fluid Mech.* **30**, 741–773.

de Lozar, A. & Hof, B. 2009 An experimental study of the decay of turbulent puffs in pipe flow. *Phil. Trans. R. Soc.* A **367**, 589–599.

Matsubara, M. & Alfredsson, P. H. 2001 Disturbance growth in boundary layers subjected to free-stream turbulence. *J. Fluid Mech.* **430**, 149–168.

Mellibovsky, F. & Meseguer, A. 2007 Pipe flow transition threshold following localized impulsive perturbations. *Phys. Fluids* **19**, 044102.

Meseguer, A. 2003 Streak breakdown instability in pipe poiseuille flow. *Phys. Fluids* **15**, 1203–1213.

Meseguer, A. & Trefethen, L. N. 2003 Linearized pipe flow to Reynolds number 10^7. *J. Comp. Phys.* **186**, 178–197.

Peixinho, J. & Mullin, T. 2006 Decay of turbulence in pipe flow. *Phys. Rev. Lett.* **96**, 094501.

Peixinho, J. & Mullin, T. 2007 Finite-amplitude thresholds for transition in pipe flow. *J. Fluid Mech.* **582**, 169–178.

Pfenniger, W. 1961 Boundary layer suction experiments with laminar flow at high Reynolds numbers in the inlet length of a tube by various suction methods. In *Boundary Layer and Flow Control* (ed. G. V. Lachman), pp. 961–980. Pergamon.

Philip, J., Svizher, A. & Cohen, J. 2007 Scaling law for subcritical transition in plane poiseuille flow. *Phys. Rev. Lett.* **98**, 154502.

Reshotko, E. & Tumin, A. 2001 Spatial theory of optimal disturbances in a circular pipe flow. *Phys. Fluids* **13** (4), 991–996.

Reynolds, O. 1883 An experimental investigation of the circumstances which determine whether motion of water shall be direct or sinous and of the law of resistance in parallel channels. *Phil. Trans. R. Soc. Lond.* **174**, 935–982.

Robinson, S. K. 1991 Coherent motions in the turbulent boundary layers. *Annu. Rev. Fluid Mech.* **23**, 601–639.

Sau, R. & Mahesh, K. 2008 Dynamics and mixing of vortex rings in crossflow. *J. Fluid Mech.* **604**, 329–354.

Schlatter, P., Brandt, L., de Lange, H. C. & Henningson, D. S. 2008 On streak breakdown in bypass transition. *Phys. Fluids* **20**, 101505.

Schmid, P. J. 2007 Nonmodal stability theory. *Annu. Rev. Fluid Mech.* **39**, 219–268.

Schmid, P. J. & Henningson, D. S. 1994 Optimal energy density growth in Hagen–Poiseuille flow. *J. Fluid Mech.* **277**, 197–225.

Suponitsky, V., Cohen, J. & Bar-Yoseph, P. Z. 2005 The generation of streaks and hairpin vortices from a localized vortex embedded in unbounded uniform shear flow. *J. Fluid Mech.* **535**, 65–100.

Svizher, A. & Cohen, J. 2006 Holographic particle image velocimetry measurements of hairpin vortices in a subcritical air channel flow. *Phys. Fluids* **18**, 014105.

Wedin, H. & Kerswell, R. R. 2004 Exact coherent structures in pipe flow: Travelling wave solutions. *J. Fluid Mech.* **508**, 333–371.

Wygnanski, I. J. & Champagne, F. H. 1973 On transition in a pipe. 1. The origin of puffs and slugs and the flow in a turbulent slug. *J. Fluid Mech.* **59**, 281–335.

Zikanov, O. Y. 1996 On the stability of pipe poiseuille flow. *Phys. Fluids* **8**, 2923–2932.